Electronic Supplementary Material (ESI) for Journal of Materials Chemistry A.

Supporting Information

Tris(pentafluorophenyl)borane-water complexes doped Spiro-TTB for high-efficiency and stable perovskite solar cells

Luyan Zhang[a,b], Jiang Sheng[b], Weichuang Yang[b], Xiangying Xue[a], Xuan Sha[b], Jingsong Sun[b,c], Chunhui Shou[c], Fangfang Cao[b], Ningjun Zhang[b], Chuanxiao Xiao[b], Xi Yang[b], Jichun Ye[b]**

[a] Faculty of Materials Science and Chemical Engineering, Ningbo University, Ningbo 315211, China

[b] Zhejiang Provincial Engineering Research Center of Energy Optoelectronic Materials and Devices, Ningbo Institute of Materials Technology & Engineering, Chinese Academy of Sciences, Ningbo 315201, China

[c] Key Laboratory of Solar Energy Utilization and Energy Saving Technology of Zhejiang Province, Zhejiang Energy Group R&D Institute Co., Ltd, Hangzhou, Zhejiang 310003, China

*Corresponding authors.

E-mail addresses: shengjiang@nimte.ac.cn(J. Sheng), jichun.ye@nimte.ac.cn (J. Ye).

Experimental Section/Methods

Materials and reagents

The organic halide salt (FAI, MAI) with a purity of > 99.9% and inorganic halide salts (CsCl, PbI_2, and $PbBr_2$) with a purity of > 99.999% were purchased from Advanced Election Technology Co., Ltd. Electron transport material of SnO_2 colloid precursor with an initial density of 15 wt% is purchased from Alfa Aesar. Hole transport material Spiro-OMeTAD with a purity of > 99% is purchased from Xi'an Polymer Light Technology. Hole transport material Spiro-TTB with a purity of > 99.55% is purchased from Luminescence Technology Corp. BCF with a purity of > 99% is purchased from Aladdin. The chlorobenzene (CB), N, Ndimethylformamide (DMF), dimethylsulphoxide (DMSO), and isopropyl alcohol (IPA) are anhydrous and purchased from Aladdin. The pre-patterned ITO glass is purchased from Advanced Election Technology Co., Ltd. The mask used for depositing metal electrodes is custom-made from Shenzhen Rigorous Technology Co., Ltd.

Precursor solution preparation

A perovskite precursor solution (1.4 м $FA_{0.82}Cs_{0.13}MA_{0.05}Pb(I_{0.80}Br_{0.20})_3$) was prepared by dissolving FAI, MAI, MACl, CsCl, PbI_2, and $PbBr_2$ in a mixed solvent (DMF/DMSO = 7:3) and then stirred at room temperature for 3 h and filtered with a 0.22 μm PTFE filter prior to use. The pristine spiro-TTB solution was prepared by dissolving 36 mg of Spiro-TTB in 1 mL of anhydrous chlorobenzene. The BCF doped Spiro-TTB solutions were prepared by mixing BCF with different contents (0 mg, 1 mg, 3 mg, 4 mg, 6 mg and 8 mg) with the pristine spiro-TTB solution. herein, the highest PCE of BCF-doped device was achieved with the 3 mg BCF. The BCF(OH_2) solutions were prepared by dissolving 3 mg BCF and water with different contents (0 μL, 0.1 μL, 0.2 μL, 0.3 μL and 0.4 μL) in 1mL anhydrous chlorobenzene, and then shaken for half an hour from colorless transparent to light pink of the solution. For the optimal ratio of BCF(OH_2) solution configuration, after 3mg BCF was completely dissolved in 1mL chlorobenzene, 0.2 μL deionized water was added. The BCF(OH_2) doped Spiro-TTB (Spiro-TTB:BA) solutions were prepared by mixing 36 mg Spiro-TTB with 1mL BCF(OH_2) solution. For semitransparent perovskite solar cells, the concentration of Spiro-TTB:BA

is half that of opaque devices. The Spiro-TTB solutions are stirred at room temperature for 48 h and filtered with a 0.22 μm PTFE filter prior to use. For Li-doped Spiro-OMeTAD solution, 17 μL of bis(trifluoromethane) sulfonamide lithium salt (Li-TFSI) stock solution (520 mg in 1mL acetonitrile), a 8 μL Tris(2-(1H-pyrazol-1-yl)-4-tertbutylpyridine)-Cobalt(III) Tris(bis-trifluoromethylsulfonykl)imide)) (FK 209 Co(III) TFSI) stock solution (360 mg in 1 mL acetonitrile)) and 73.5 mg Spiro-OMeTAD was added into 1 mL of chlorobenzene. The Spiro-OMeTAD solutions are stirred at room temperature for 12 h and filtered with a 0.22 μm PTFE/ filter prior to use. All the materials and reagents are used as received without further purification.

Device fabrication

The pre-patterned ITO glass was sequentially cleaned by ultrasonic cleaning in detergent, acetone, and ethanol for 15 min, respectively. After that, the ITO glass with residual ethanol was dried in a vacuum drying oven at 70°C for 30 min and then cleaned with ultraviolet ozone for 15 min to improve the surface wetting. To deposit ETL, the cleaned ITO glasses were spin-coated with a thin layer of SnO_2 nanoparticle film (3.75%, diluted by deionized water) at 4,000 r.p.m for 30 s, filtered with a 0.45 μm PTFE filter prior to use, and annealed in ambient air at 150°C for 30 min. Then, the samples were transferred into the nitrogen glove box to fabricate the perovskite layer through a one-step film formation method: A 70 μL sample of perovskite solution was spun onto the substrates at 1,000 rpm for 8 s and 5,000 rpm for 30 s. Chlorobenzene (300 μL) was dropped in the center of the substrates 10 s before the end of the spin-coating process. After the rotation ceased, the substrates were immediately transferred onto a hot plate of 110°C and annealed for 30 min. Then, the HTL was deposited by spin-coating Spiro-TTB/ Spiro-OMeTAD solution at 3,000 r.p.m. for 30 s. Subsequently, semi-finished devices were stored in an auto-drying cabinet at 25°C with a relative humidity of < 3% over night. For opaque perovskite solar cells, a 80 nm thick Au layer was deposited onto the HTL by the thermal evaporation. For semitransparent perovskite solar cells, 10 nm MoO_3 was deposited on the HTL by thermal evaporation to construct the buffer layer, after which a 100 nm-thick indium zinc oxide (IZO) layer was deposited by sputtering at room temperature with a radio

frequency power of 80 W. Finally, 80 nm Au was evaporated around the IZO pads through a mask defining a U-shaped busbar.

Characterization

The current–voltage (J-V) measurements were carried out by using a Keysight B2901A Source Meter under simulated one-sun AM 1.5G illumination (100 mW cm^{-2}) with a solar simulator (Enlitech, SS-F5-3A, China) in ambient air without encapsulation. The active area calibrated with shadow mask is approximately 0.1 cm2. The voltage was swept both in forward scan (1.2 V to 0.1 V, step 0.01 V) and reverse scan (-0.1 V to 1.2 V, step 0.01 V) with 10 ms delay time. The space-charge-limited current (SCLC) measurements were carried out in the same equipment under dark condition. The external quantum efficiency (EQE) spectra were measured using a solar cell spectrum response measurement system (Enlitech, QE-R3011, China) of which the light intensity at each wavelength was calibrated by a standard Si detector. The fourier transform infrared (FTIR) measurements were measured in transmission mode by a NICOLET 6700 (THermo, USA) spectrometer equipped with a DLATGS detector. The optical absorption and transmittance spectra were obtained by using a Lambda 950 UV/Vis/NIR spectrophotometer (Perkin-Elmer, USA). The ^{19}F nuclear magnetic resonance (NMR) spectra were measured by AVANCE NEO 600 (Bruker, Switzerland). The electron spin resonance (ESR) spectroscopy was measured by Electron spin magnetic resonance Spectrometer (E500) (Bruker, Germany). The ultra-violet photoelectron spectroscopy (UPS) was carried out under ultra-high vacuum with a monochromatic Al Ka X-ray source (AXIS SUPRA, Kratos). X-ray diffraction (XRD) patterns were obtained on a AXS D8 Advance (Bruker, Germany). The scanning electron microscopy (SEM) images were captured by a field-emission S4800 SEM (Hitachi, Japan). The steady-state photoluminescence (SSPL) spectra were obtained by FL3-111 spectrometer (HORIBA, French) and time-resolved photoluminescence (TRPL) spectra were measured using an FLS1000 (Edinburgh, UK). Dimension ICON SPM (Bruker, USA) was used to characterize the surface potentials and c-afm. The thermal gravity (TG) loss curves were obtained by TG209F1 (NETZSCH，Germany). The differential scanning calorimetry (DSC) were carried out under TG-DSC STA 449F3

(NETZSCH, Germany). The hall mobility were conducted by 8404-CRX-6.5K (LakeShore, USA). The surface tension/dynamic contact angle measurement were captured by DCAT21 (Jin Mao, China). The transient photovoltage (TPV) decay measurements, capacitance-voltage (CV) measurements and electrochemical impedance spectroscopy (EIS) were recorded by electrochemical workstation CHI660 (Zahner, Germany) with an 80 mW cm^{-2} white light illuminated. For the operational stability, the continuous power outputs of the encapsulated solar cells were applied bias at the MPP condition by Keithley 2400 source meter under a 100 mW cm^{-2} Xenon lamp without additional optical filter.

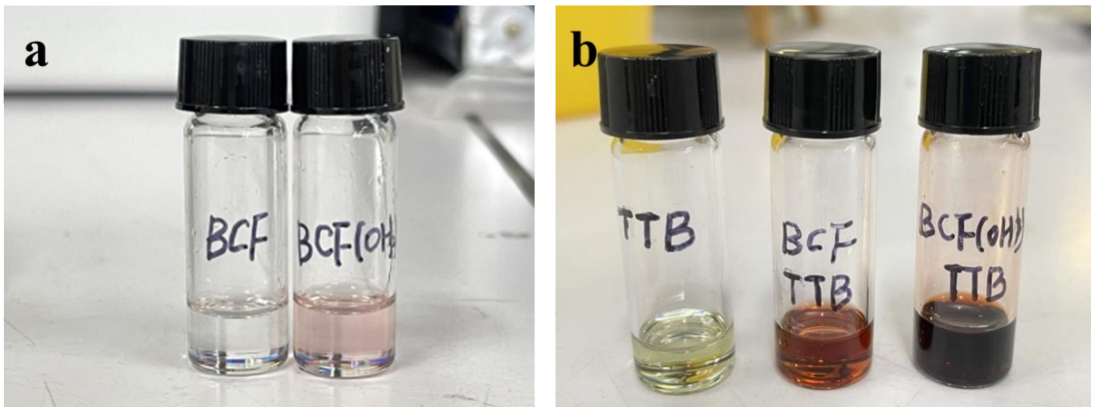

Figure S1. Photos of the (a) BCF and BCF-H_2O, (b) pristine Spiro-TTB, BCF-doped Spiro-TTB (Spiro-TTB:LA) and BCF(OH_2)-doped Spiro-TTB (Spiro-TTB:BA) solutions.

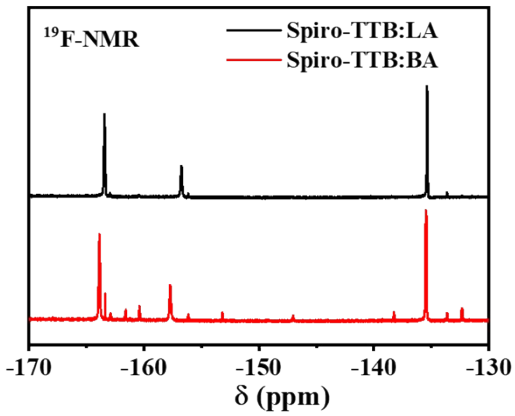

Figure S2. ^{19}F NMR spectra of Spiro-TTB:BA and Spiro-TTB:LA dissolved in CB-D5 solutions.

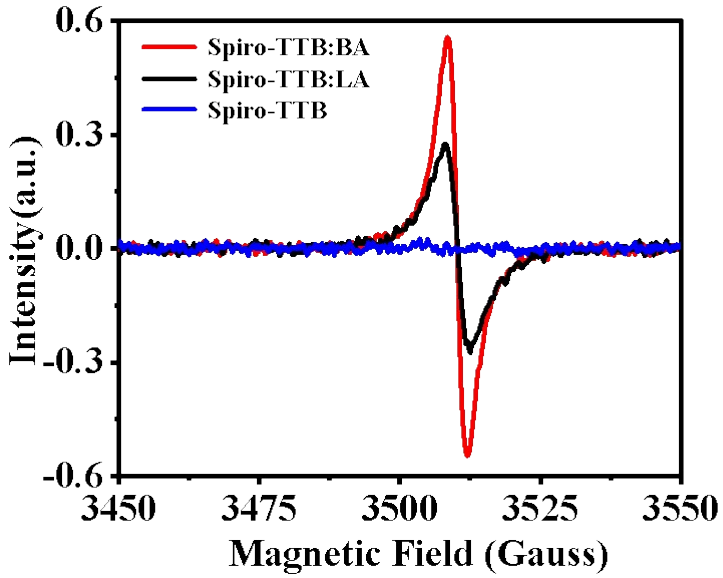

Figure S3. ESR spectra of pure spiro-TTB and BCF and BCF(OH_2)doped spiro-OMeTAD.

ESR spectra are used to study the electron transfer between the OSC material and BCF molecules, which has been added in supporting information (Figure S3). ESR spectroscopy is a sensitive, specific method for the identification and study of free radicals. In order to confirm the presence of an unpaired electron in spiro-TTB, we performed the ESR measurement of the spiro-TTB films without and with BCF, BCF(OH_2) doping. As can be seen from Figure S3, no paramagnetic signal is detected in the undoped Spiro-TTB film, while the obvious paramagnetic signals at a magnetic field of around 3508 G are presented in the doped Spiro-TTB, indicating that the presence of the unpaired electron of a $[Spiro\text{-}TTB]^{\bullet+}$ radical under the BCF and BCF(OH_2) doping. Thus, there is an electron transfer from the Spiro-TTB to BCF/BCF(OH_2) molecule. Moreover, the BCF(OH_2)-doped spiro-TTB film presents stronger paramagnetic signal compared with that of BCF-doped spiro-TTB film. The increased ESR signal is reasonably attributed to the more radical cations of spiro-TTB. This implies that the Brønsted acid (BCF(OH_2)) doping may lead to much more efficient doping of Spiro-TTB compared to the Lewis acid (BCF) doping through the mechanisms as illustrated in our proposed scheme.

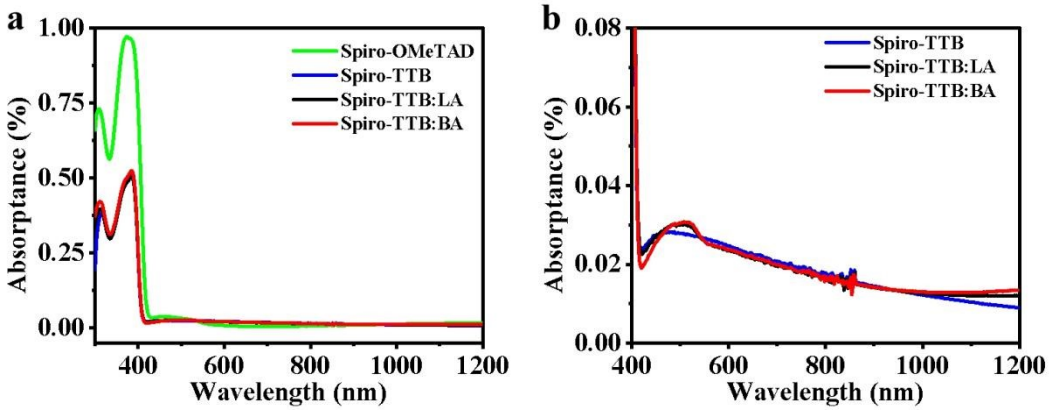

Figure S4. (a) UV-vis spectra of undoped, BCF-doped, and BCF(OH_2)-doped spiro-TTB and Spiro-OMeTAD films coated on the quartz glass. (72 mg/mL Spiro-OMeTAD, 36 mg/mL Spiro-TTB). (b)UV-vis of partial spectra of undoped, BCF-doped, and BCF(OH_2)-doped spiro-TTB films coated on quartz glass.

Table S1. Hall mobilities of Spiro-TTB films

Sample	Spiro-TTB:BA	Spiro-TTB:LA	Spiro-TTB
Hall mobility [$cm^2 \cdot V^{-1} \cdot s^{-1}$]	1.22×10^{-2}	6.1×10^{-3}	4.12×10^{-4}

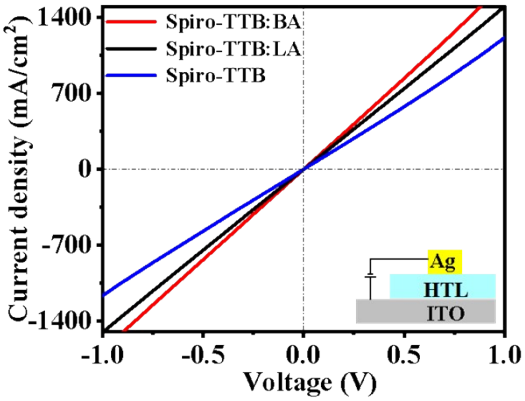

Figure S5. *J-V* curves of the hole-only devices to evaluate the hole transporting capability of the buried layers (the device configuration is shown in the inset).

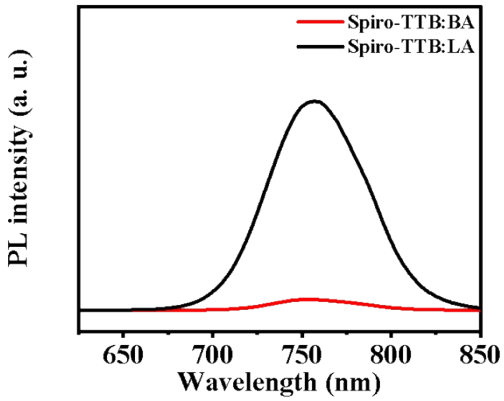

Figure S6. Steady-state PL spectra of Spiro-TTB:BA and Spiro-TTB:LA layers deposited on perovskite-coated ITO/glass substrates under excitation wavelength of 470 nm.

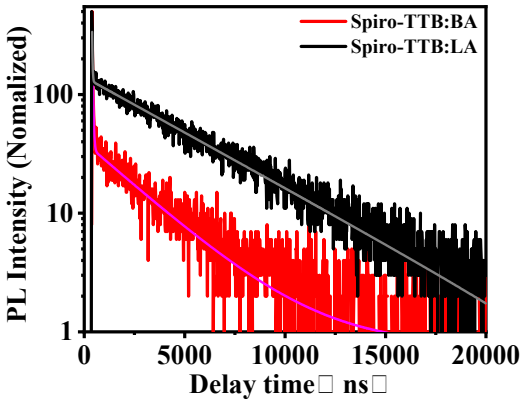

Figure S7. TRPL spectra of Spiro-TTB:BA and Spiro-TTB:LA layers coated on a Perovskite film under excitation wavelength of 470 nm. The extinction of TRPL intensity is often considered a measure of effective charge extraction. The TRPL intensity of Spiro-TTB:BA is much lower than that of Spiro-TTB:LA when Spiro-TTB BA is coated on the perovskite surface as HTL, while the τ_1 (corresponds to the free charge carrier transport from the perovskite layer to the HTL) and τ_2 (represents the bulk recombination of perovskite layer) are determined to be 50.4 and 11628 ns for the Spiro-TTB:LA sample, and 35.25 and 2906 ns for the Spiro-TTB:BA sample, respectively. This indicates that the addition of water makes the BCF doping more effective, the hole extraction ability of Spiro-TTB:BA is better, and the carrier transport is more efficient. The tendency is in line with the results from the perovskite side excitation.

Table S2. A brief summary of the non-lithium dopants for the Spiro.

Dopant		V_{OC} (V)	J_{SC} (mA/cm^2)	FF (%)	PCE (%)	Ref
CuPC	2015	1.135	22.6	75.45	19.35	[1]
CuSCN/CuI	2016	1.06	22.1	77	18.02	[2]
Mo(tfd-$CO_2Me)_3$	2017	1.06	21.98	74	17.2	[3]
Mo(tfd-$COCF_3)_3$	2017	1.07	22.11	76	17.8	[3]
F4-TCNQ	2017	0.92	19.04	73	12.93	[4]
BMPyTFSI	2018	1.02	21.17	65	14.06	[5]
$Cu(TFSI)_2$	2019	1	20.79	66.42	13.4	[6]
pedot	2019	1.17	21.6	72.8	18.3	[7]
F4TCNQ	2019	1.01	24.97	71.6	18.13	[8]
TPFB	2020	1.14	13.44	75.29	20.13	[9]
PHC	2021	1.11	23.92	80.24	21.34	[10]
$Zn(TFSI)_2$+tBP	2021	1.15	24.4	79	22%	[11]
FK209	2022	1.10	24.25	73	19.62	[12]
F4TCNQ	2022	1.09	20.7	64.8	14.6	[13]
BPO	2022	1.11	22.6	73	18.3	[14]
spiro-OMeTAD2$^{\bullet+}$($TFSI^-$ $)_2$+$TBMP^+TFSI^-$	2022	1.17	25.52	83.88	25.1	[15]
BCF(OH_2)		1.15	21.97	82.22	20.86	This work

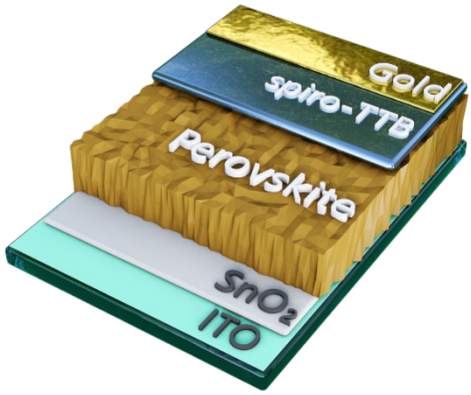

Figure S8. Device structures of PSC.

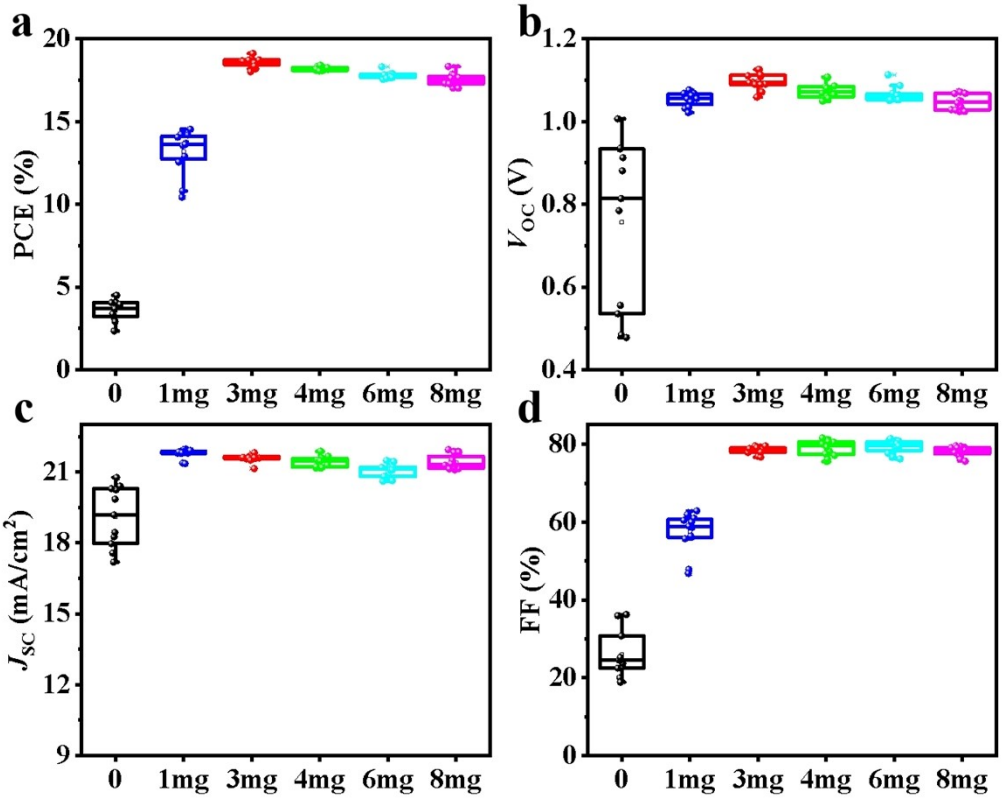

Figure S9. (a) PCE, (b) V_{OC}, (c) J_{SC} and (d) FF statistical diagrams of the PSC with different contents of BCF (0, 1mg, 3mg, 4mg, 6mg, 8mg). The Spiro-TTB is 36 mg and CB is 1 mL. The data are obtained from 11 individual cells. The device PCE is highest when the BCF is 3 mg, then as the BCF concentration increases, the V_{OC} gradually decreases and so does the PCE.

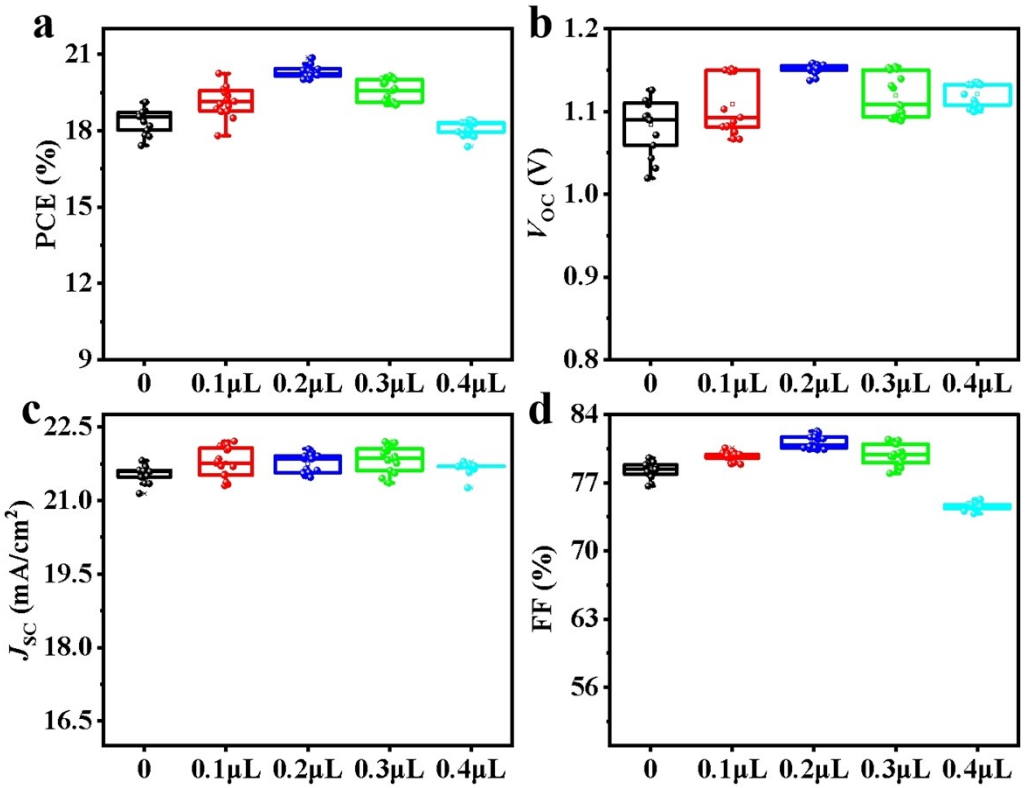

Figure S10. The distributions of photovoltaic properties (a) PCE, (b) V_{OC}, (c) J_{SC} and (d) FF of PSCs with the different contents of water (0 μL, 0.1 μL, 0.2 μL, 0.3 μL and 0.4 μL)**.** The Spiro-TTB is 36mg and BCF is 3mg. The highest device PCE is achieved with the addition of 0.2 μL water.

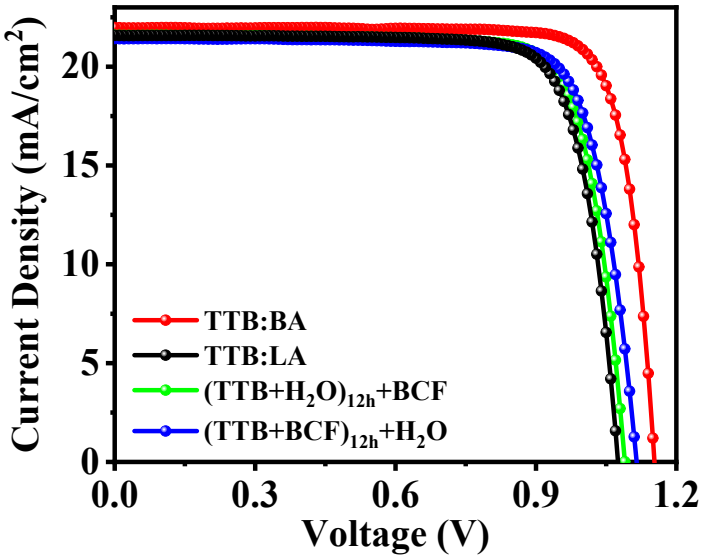

Figure S11. *J-V* curves of the opaque PSCs with Spiro-TTB:LA, Spiro-TTB:BA, $(TTB+H_2O)_{12h}$+BCF and $(TTB+BCF)_{12h}+H_2O$. $(TTB+H_2O)_{12h}$+BCF means that TTB and water are first stirred together before adding BCF, $(TTB+BCF)_{12h}+H_2O$ means that TTB and BCF are first stirred for 12h before adding water. It can be seen that Spiro-TTB:BA has the highest PSC efficiency, indicating the highest doping efficiency of BCF(OH_2) and Spiro-TTB.

Table S3. Photovoltaic parameters for Spiro-TTB:LA, Spiro-TTB:BA $(TTB+H_2O)_{12h}$+BCF and $(TTB+BCF)_{12h}+H_2O$ corresponding PSCs.

	V_{OC} (V)	J_{SC} (mA/cm^2)	FF (%)	PCE (%)
TTB:BA	1.15	21.97	82	20.86
TTB:LA	1.09	21.59	79.55	18.72
$(TTB+H_2O)_{12h}$+BCF	1.07	21.57	79.30	18.40
$(TTB+BCF)_{12h}+H_2O$	1.11	21.41	79.29	18.93

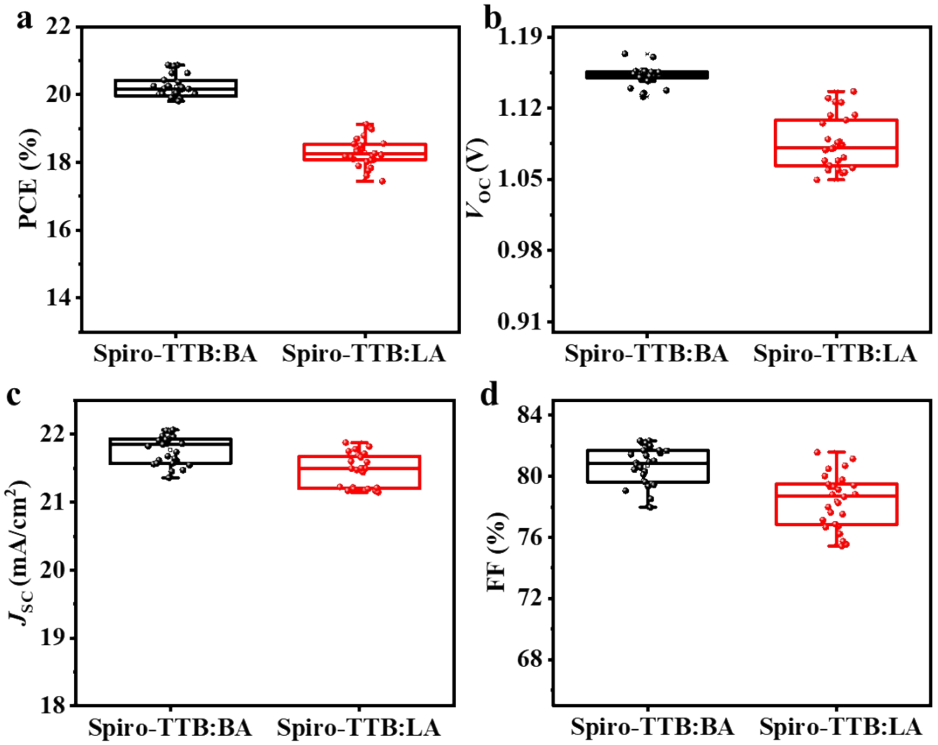

Figure S12. (a) PCE, (b) V_{OC}, (c) J_{SC}, and (d) FF statistical distributions of the optimal Spiro-TTB:BA and Spiro-TTB:LA-based devices.

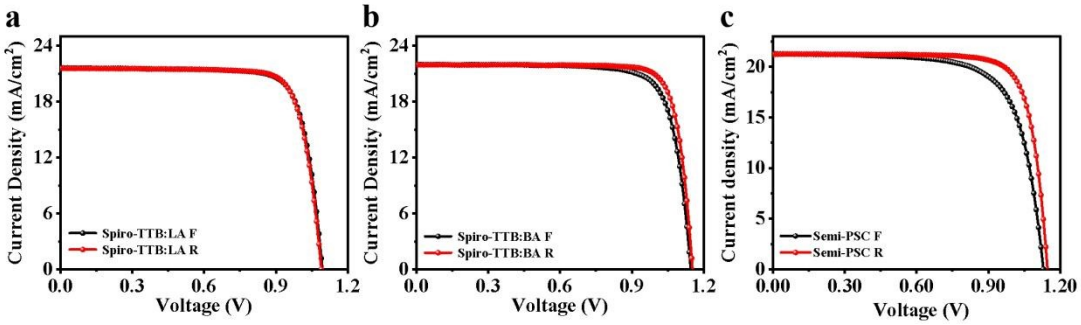

Figure S13. *J-V* curves of the opaque PSCs with (a) Spiro-TTB:LA, (b) Spiro-TTB:BA layers. (c) *J-V* curves of the ST-PSCs with Spiro-TTB:BA layer.

Table S4. Photovoltaic parameters for Spiro-TTB:LA, Spiro-TTB:BA PSCs and Spiro-TTB:BA ST-PSC.

Sample		V_{OC} (V)	J_{SC} (mA/cm^2)	FF (%)	PCE (%)
Spiro-TTB:LA	F	1.09	21.6	78.8	18.65
	R	1.09	21.5	79.5	18.72
Spiro-TTB:BA	F	1.14	22	78.5	19.81
	R	1.15	21.9	82.33	20.86
ST-PSC based on Spiro-TTB:BA	F	1.13	21.29	71.46	17.19
	R	1.14	21.29	79.43	19.35

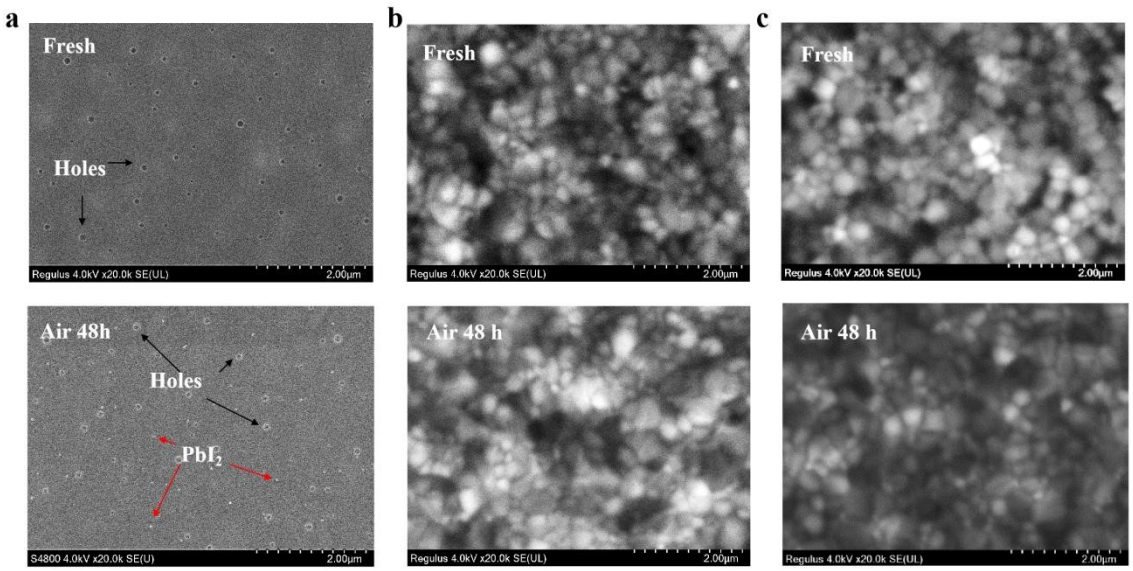

Figure S14. Original SEM images of (a) Spiro-OMeTAD, (b) Spiro-TTB:BA and (c) Spiro-TTB:LA layers deposited on perovskite-coated ITO/glass substrates freshly prepared (above) and stored in air (below, humidity about 65-90%) for 48 h.

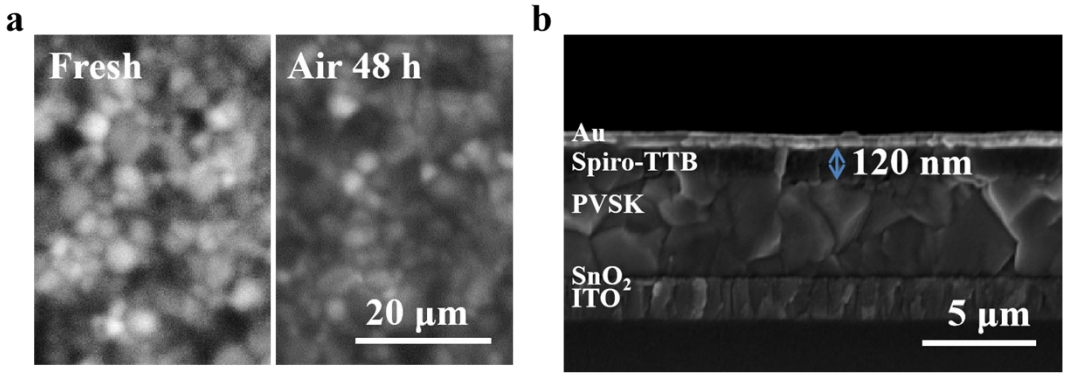

Figure S15. (a) Top-view SEM images of Spiro-TTB:LA layer deposited on perovskite-coated ITO/glass substrates freshly prepared and placed in air (65-90% RH) for 48 h. (b) Cross-sectional SEM image of the opaque PSCs used in this work. Perovskite film under Spiro-TTB:LA HTL didn't decomposed in air (65-90% RH) for 48 h.

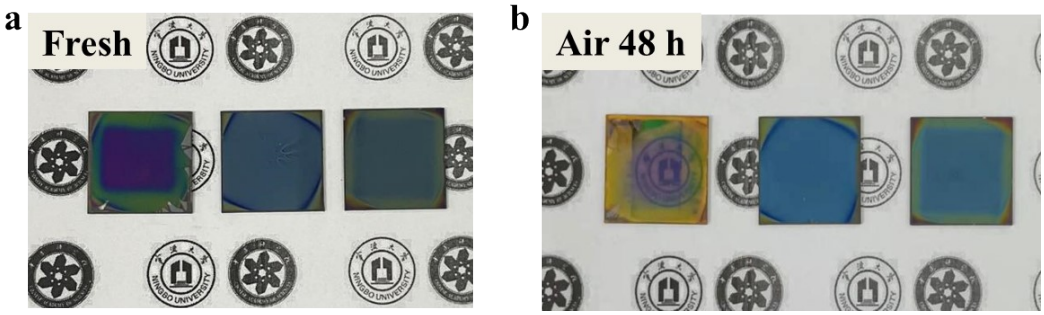

Figure S16. Photos of the Spiro-OMeTAD, Spiro-TTB:BA and Spiro-TTB:BA deposited on perovskite-coated ITO/glass substrates under (a) fresh and after (b) Air atmosphere (65-90% RH) 48 h. The Spiro-OMeTAD devices decomposed significantly when left at 65-90% RH for 48 h. The Spiro-TTB:BA and Spiro-TTB:LA devices appeared unchanged, indicating the excellent wet stability of BCF(OH_2) as a dopant.

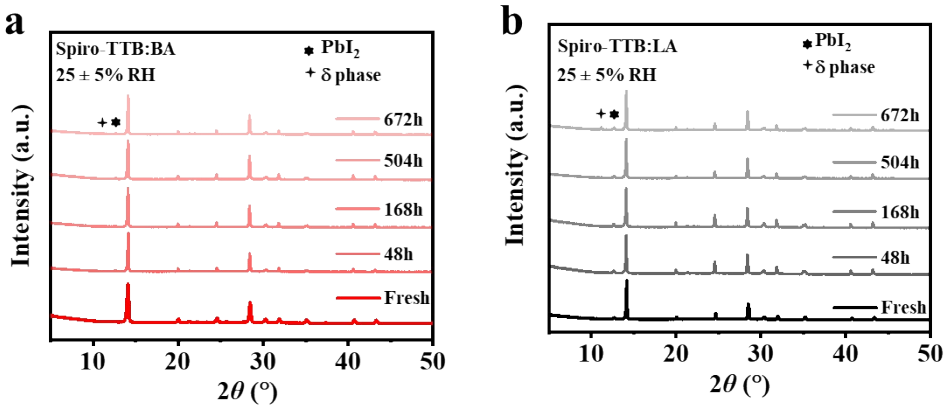

Figure S17. XRD spectra of (a) spiro-TTB:BA, (b) Spiro-TTB:LA film deposited on perovskite-coated ITO/glass substrates, after storing at room temperature and 25 ± 5% RH.

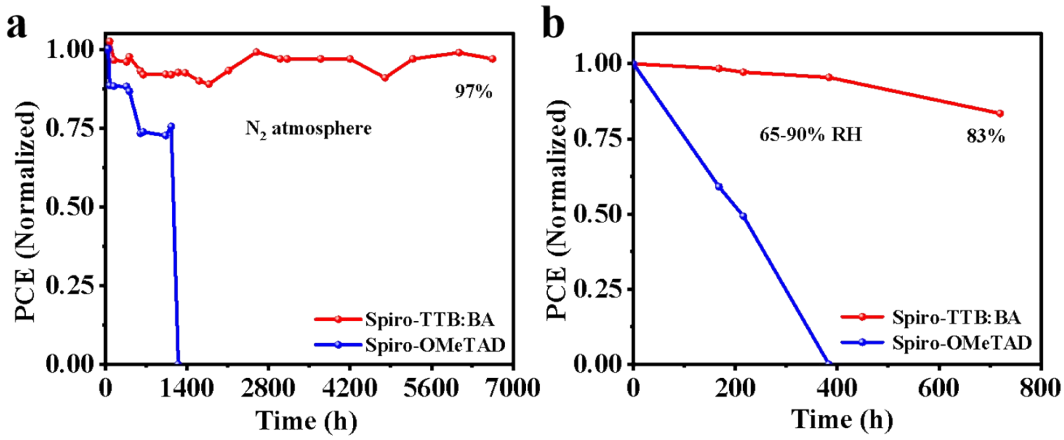

Figure S18. Long-term air stability of unencapsulated solar cells (a) Deposited in Glove Box (N_2, RH < 0.01%) and (b) at air with relative 65-90% RH. The Spiro-TTB:BA device retains 97% of its initial efficiency after 6648 h in the glove box and 83% of its initial efficiency after 720 h in air, which is significantly better than the corresponding Spiro-OMeTAD.

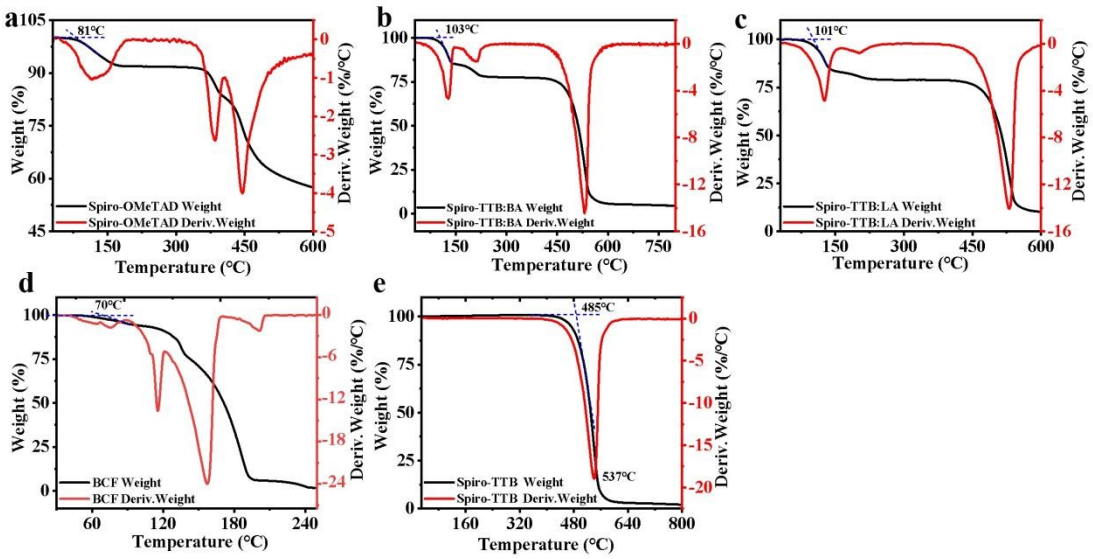

Figure S19. TGA curves of (a) Spiro-OMeTAD, (b) Spiro-TTB:BA, (c) Spiro-TTB:LA, (d)BCF, (e) pure Spiro-TTB powders. The decomposition temperature was measured by using an extrapolation starting point method on the basis of international standard ISO 11358. The point of intersection of the tangent line at the level of the front of the TG step and the tangent line at the inflection point of the curve can be used as a reference temperature point for the onset of the weightlessness process. The decomposition point could be obtained from the TG curve, which directly determine the maximum working temperature of the Spiro-TTB or Spiro-OMeTAD. Spiro-TTB:BA starts to decompose at around 103°C, whereas the Li-TFSI doped Spiro-OMeTAD starts to decompose at 81°C, indicating that Spiro-TTB:BA has better thermal stability.

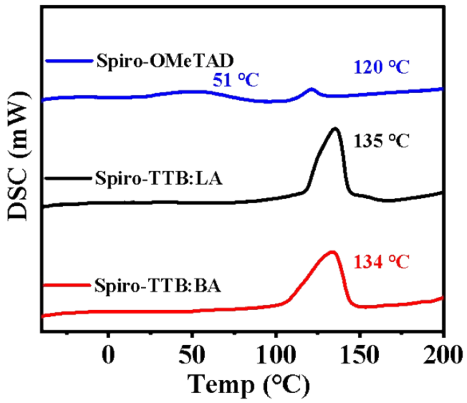

Figure S20. DSC curves of Spiro-TTB:BA, Spiro-TTB:LA and Spiro-OMeTAD powders. Spiro-OMeTAD has a small endothermic peak at 51°C, indicating that the crystal structure of Spiro-OMeTAD has changed in some way to possibly cause the instability. In addition, the main endothermic peak of Spiro-OMeTAD is at 120 °C, while the endothermic peak temperatures of both Spiro-TTB:BA and Spiro-TTB:LA are 135 °C, indicating a significant thermal decomposition reaction at this time, which is consistent with the TG curve.

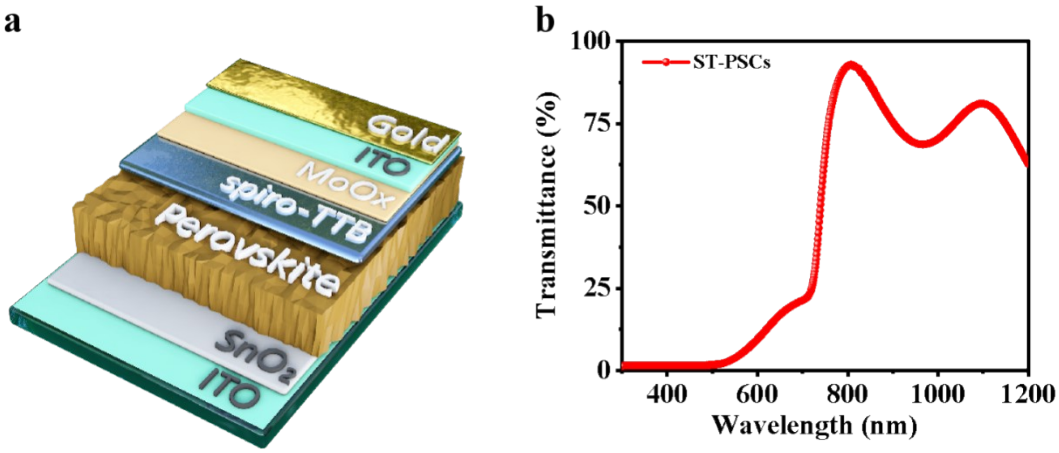

Figure S21. (a) The structure of semitransparent device. (b) Transmittance of ST-PSCs.

Table S5. Summary of n-i-p ST-PSCs (with the efficiency above 16%) reported in the literatures.

Data	V_{OC} (V)	J_{SC} (mA/cm^2)	FF (%)	PCE (%)	*E*g (eV)	Ref.
2016/7/30	1.07	20.1	76.1	16.4	x	[16]
2016/11/4	1.10	21.5	73.5	17.4	1.5	[17]
2019/8/23	1.06	21.52	77.5	17.7	1.58	[18]
2019/11/4	1.15	19.8	79.9	18.3	1.53	[19]
2020/1/31	1.20	18.00	78.9	17.1	1.72	[20]
2020/2/19	1.12	22.30	77.7	19	1.63	[21]
2020/4/2	1.02	23.5	78.8	18.9	1.56	[22]
2020/5/14	1.12	22.7	73.8	18.8	x	[23]
2020/6/22	1.10	20.63	73.6	16.72	1.7	[24]
2020/9/29	1.12	22.7	73.8	18.8	1.59	[25]
2021/2/12	1.05	21.50	76.9	17.37	x	[26]
2021/2/25	1.13	21.9	79.7	19.8	1.52	[27]
2021/6/14	1.06	22.8	73.2	17.8	x	[28]
2021/6/26	1.06	21.74	77.4	17.9	x	[29]
2022/2/8	1.104	23.9	71.0	18.7	x	[30]
2022.7.1	1.08	23.33	77.28	19.48	1.55	[31]
2022.7.7	1.186	19.57	80.56	18.7	1.67	[32]
2022.7.27	1.24	18.82	79.58	18.57	1.77	[33]
2022.9.29	1.17	20.7	79	18.5	1.62	[34]
This work	**1.14**	**21.29**	**79.43**	**19.35**	**1.65**	

Table S6. Summary of n-i-p 4-T perovskite/silicon tandems (with the PCE above 25%) reported in the literatures.

Data	Top cell PCE(%)	Area (cm^2)	Eg (eV)	Bottom cell PCE (%)	Total PCE(%)	Ref.
2016/7/30	16.4	0.25	x	8.8	25.2	[16]
2017/4/4	16.0	0.16	1.73	10.4	26.4	[35]
2018/12/12	13.8	0.13	1.72	13.3	27.1	[36]
2019/8/23	17.7	0.09	1.58	7.8	25.5	[18]
2019/11/4	18.3	0.096	1.53	8.7	27	[37]
2020/1/31	17.0	0.21	1.72	10.7	27.7	[20]
2020/4/2	18.9	0.07	1.56	7.1	26	[22]
2021/2/25	19.8	x	1.52	8.5	28.3	[27]
2021/6/14	17.8	0.07	x	8.3	26.1	[28]
2022/7/7	18.7	x	1.67	8.65	27.35	[32]
2022/7/27	18.57	x	1.77	11.67	30.24	[33]
This work	**19.35**	**0.09**	**1.65**	**8.47**	**27.82**	

References

1. J. Seo, N. J. Jeon, W. S. Yang, H. W. Shin, T. K. Ahn, J. Lee, J. H. Noh and S. I. Seok, *Adv. Energy Mater.*, 2015, **5**, 1501320.
2. M. Li, Z. K. Wang, Y. G. Yang, Y. Hu, S. L. Feng, J. M. Wang, X. Y. Gao and L. S. Liao, *Adv. Energy Mater.*, 2016, **6**, 1601156.
3. A. Pellaroque, N. K. Noel, S. N. Habisreutinger, Y. Zhang, S. Barlow, S. R. Marder and H. J. Snaith, *ACS Energy Lett.*, 2017, **2**, 2044-2050.
4. J. Luo, C. Jia, Z. Wan, F. Han, B. Zhao and R. Wang, *J. Power Sources*, 2017, **342**, 886-895.
5. L. Calio, M. Salado, S. Kazim and S. Ahmad, *Joule*, 2018, **2**, 1800-1815.
6. J. Mohanraj, M. Stihl, E. Simon, O. von Sicard, G. Schmidt, M. Fleischer, C. Neuber and M. Thelakkat, *ACS Appl. Energy Mater.*, 2019, **2**, 3469-3478.
7. L. Kegelmann, P. Tockhorn, C. M. Wolff, J. A. Márquez, S. n. Caicedo-Dávila, L. Korte, T. Unold, W. Lövenich, D. Neher and B. Rech, *ACS Appl. Energy Mater.*, 2019, **11**, 9172-9181.
8. K. Guo, M. Wu, S. Yang, Z. Wang, J. Li, X. Liang, F. Zhang, Z. Liu and Z. Wang, *Sol. RRL*, 2019, **3**, 1800352.
9. J. Liu, W. Liu, E. Aydin, G. T. Harrison, F. H. Isikgor, X. Yang, A. S. Subbiah and S. De Wolf, *ACS Appl. Energy Mater.*, 2020, **12**, 23874-23884.
10. J. Xia, R. Zhang, J. Luo, H. Yang, H. Shu, H. A. Malik, Z. Wan, Y. Shi, K. Han, R. Wang, X. Yao and C. Jia, *Nano Energy*, 2021, **85**, 106018.
11. G. Zhu, L. Yang, C. Zhang, G. Du, N. Fan, Z. Luo, X. Zhang and J. Zhang, *ACS Appl. Energy Mater.*, 2022, **5**, 3595-3604.
12. M. Liu, S. Dahlström, C. Ahläng, S. Wilken, A. Degterev, A. Matuhina, M. Hadadian, M. Markkanen, K. Aitola and A. Kamppinen, *J. Mater. Chem. A*, 2022, **10**, 11721-11731.
13. Y. Zhang, B. Huang, M. Hu, B. Tan, F. Huang, Y.-B. Cheng, A. N. Simonov and J. Lu, *J. Mater. Chem. A*, 2022, **10**, 10604-10613.

1. J. Seo, N. J. Jeon, W. S. Yang, H. W. Shin, T. K. Ahn, J. Lee, J. H. Noh and S. I. Seok, *Adv. Energy Mater.*, 2015, **5**, 1501320.
2. M. Li, Z. K. Wang, Y. G. Yang, Y. Hu, S. L. Feng, J. M. Wang, X. Y. Gao and L. S. Liao, *Adv. Energy Mater.*, 2016, **6**, 1601156.
3. A. Pellaroque, N. K. Noel, S. N. Habisreutinger, Y. Zhang, S. Barlow, S. R. Marder and H. J. Snaith, *ACS Energy Lett.*, 2017, **2**, 2044-2050.
4. J. Luo, C. Jia, Z. Wan, F. Han, B. Zhao and R. Wang, *J. Power Sources*, 2017, **342**, 886-895.
5. L. Calio, M. Salado, S. Kazim and S. Ahmad, *Joule*, 2018, **2**, 1800-1815.
6. J. Mohanraj, M. Stihl, E. Simon, O. von Sicard, G. n. Schmidt, M. Fleischer, C. Neuber and M. Thelakkat, *ACS Appl. Energy Mater.*, 2019, **2**, 3469-3478.
7. L. Kegelmann, P. Tockhorn, C. M. Wolff, J. A. Márquez, S. n. Caicedo-Dávila, L. Korte, T. Unold, W. Lövenich, D. Neher and B. Rech, *ACS Appl. Energy Mater.*, 2019, **11**, 9172-9181.
8. K. Guo, M. Wu, S. Yang, Z. Wang, J. Li, X. Liang, F. Zhang, Z. Liu and Z. Wang, *Sol. RRL*, 2019, **3**, 1800352.
9. J. Liu, W. Liu, E. Aydin, G. T. Harrison, F. H. Isikgor, X. Yang, A. S. Subbiah and S. De Wolf, *ACS Appl. Energy Mater.*, 2020, **12**, 23874-23884.
10. J. Xia, R. Zhang, J. Luo, H. Yang, H. Shu, H. A. Malik, Z. Wan, Y. Shi, K. Han, R. Wang, X. Yao and C. Jia, *Nano Energy*, 2021, **85**, 106018.

11. J. Y. Seo, S. Akin, M. Zalibera, M. A. R. Preciado, H. S. Kim, S. M. Zakeeruddin, J. V. Milić and M. Grätzel, *Adv. Funct. Mater.*, 2021, **31**, 2102124.
12. G. Zhu, L. Yang, C. Zhang, G. Du, N. Fan, Z. Luo, X. Zhang and J. Zhang, *ACS Appl. Energy Mater.*, 2022, **5**, 3595-3604.
13. M. Liu, S. Dahlström, C. Ahläng, S. Wilken, A. Degterev, A. Matuhina, M. Hadadian, M. Markkanen, K. Aitola and A. Kamppinen, *J. Mater. Chem. A*, 2022, **10**, 11721-11731.
14. Y. Zhang, B. Huang, M. Hu, B. Tan, F. Huang, Y.-B. Cheng, A. N. Simonov and J. Lu, *J. Mater. Chem. A*, 2022, **10**, 10604-10613.
15. T. Zhang, F. Wang, H.-B. Kim, I.-W. Choi, C. Wang, E. Cho, R. Konefal, Y. Puttisong, K. Terado and L. Kobera, *Science*, 2022, **377**, 495-501.
16. J. Werner, L. Barraud, A. Walter, M. Bräuninger, F. Sahli, D. Sacchetto, N. Tétreault, B. Paviet-Salomon, S.-J. Moon, C. Allebé, M. Despeisse, S. Nicolay, S. De Wolf, B. Niesen and C. Ballif, *ACS Energy Lett.*, 2016, **1**, 474-480.
17. J. Peng, T. Duong, X. Zhou, H. Shen, Y. Wu, H. K. Mulmudi, Y. Wan, D. Zhong, J. Li and T. Tsuzuki, *Adv. Energy Mater.*, 2017, **7**, 1601768.
18. H. A. Dewi, H. Wang, J. Li, M. Thway, R. Sridharan, R. Stangl, F. Lin, A. G. Aberle, N. Mathews, A. Bruno and S. Mhaisalkar, *ACS Appl. Energy Mater.*, 2019, **11**, 34178-34187.
19. B. Chen, S.-W. Baek, Y. Hou, E. Aydin, M. De Bastiani, B. Scheffel, A. Proppe, Z. Huang, M. Wei and Y.-K. Wang, *Nat. Commun.*, 2020, **11**, 1-9.
20. T. Duong, H. Pham, T. C. Kho, P. Phang, K. C. Fong, D. Yan, Y. Yin, J. Peng, M. A. Mahmud and S. Gharibzadeh, *Adv. Energy Mater.*, 2020, **10**, 1903553.
21. B. Chen, S.-W. Baek, Y. Hou, E. Aydin, M. De Bastiani, B. Scheffel, A. Proppe, Z. Huang, M. Wei, Y.-K. Wang, E.-H. Jung, T. G. Allen, E. Van Kerschaver, F. P. García de Arquer, M. I. Saidaminov, S. Hoogland, S. De Wolf and E. H. Sargent, *Nat. Commun.*, 2020, **11**, 1257.
22. H. H. Park, J. Kim, G. Kim, H. Jung, S. Kim, C. S. Moon, S. J. Lee, S. S. Shin, X. Hao and J. S. Yun, *Small Methods*, 2020, **4**, 2000074.
23. I. Jeon, A. Shawky, S. Seo, Y. Qian, A. Anisimov, E. I. Kauppinen, Y. Matsuo and S. Maruyama, *J. Mater. Chem. A*, 2020, **8**, 11141-11147.
24. R. A. Jagt, T. N. Huq, S. A. Hill, M. Thway, T. Liu, M. Napari, B. Roose, K. Gałkowski, W. Li, S. F. Lin, S. D. Stranks, J. L. MacManus-Driscoll and R. L. Z. Hoye, *ACS Energy Lett.*, 2020, **5**, 2456-2465.
25. C. Lee, S.-W. Lee, S. Bae, A. Shawky, V. Devaraj, A. Anisimov, E. I. Kauppinen, J.-W. Oh, Y. Kang, D. Kim, I. Jeon, S. Maruyama and H.-S. Lee, *Sol. RRL*, 2020, **4**, 2000353.
26. A. Andruszkiewicz, X. Zhang, M. B. Johansson, L. Yuan and E. M. Johansson, *Nanoscale*, 2021, **13**, 6234-6240.
27. D. Yang, X. Zhang, Y. Hou, K. Wang, T. Ye, J. Yoon, C. Wu, M. Sanghadasa, S. F. Liu and S. Priya, *Nano Energy*, 2021, **84**, 105934.
28. H. Jung, G. Kim, G. S. Jang, J. Lim, M. Kim, C. S. Moon, X. Hao, N. J. Jeon, J. S. Yun and H. H. Park, *ACS Appl. Energy Mater.*, 2021, **13**, 30497-30503.
29. U. Gunes, E. Bag Celik, C. C. Akgul, M. Koc, M. Ameri, B. E. Uzuner, M. Ghasemi, M. C. Sahiner, İ. Yildiz and H. Z. Kaya, *Adv. Funct. Mater.*, 2021, **31**, 2103130.
30. C. Zhang, M. Chen, F. Fu, H. Zhu, T. Feurer, W. Tian, C. Zhu, K. Zhou, S. Jin and S. M. Zakeeruddin, *Energy Environ. Sci.*, 2022, **15**, 1536-1544.
31. M. J. Jeong, J. H. Lee, C. H. You, S. Y. Kim, S. Lee and J. H. Noh, *Adv. Energy Mater.*, 2022, **12**.

32. J. Accounts of chemical researchTao, X. Liu, J. Shen, S. Han, L. Guan, G. Fu, D.-B. Kuang and S. Yang, *ACS Nano*, 2022, **16**, 10798-10810.
33. Y. Yao, P. Hang, B. Li, Z. Hu, C. Kan, J. Xie, Y. Wang, Y. Zhang, D. Yang and X. Yu, *Small*, 2022, **18**, e2203319.
34. T. Feeney, I. M. Hossain, S. Gharibzadeh, F. Gota, R. Singh, P. Fassl, A. Mertens, A. Farag, J.-P. Becker, S. Paetel, E. Ahlswede and U. W. Paetzold, *Sol. RRL*, 2022, **6**.
35. D. The, Y. Wu, H. Shen, J. Peng, X. Fu, D. Jacobs, E.-C. Wang, T. C. Kho, K. C. Fong, M. Stocks, E. Franklin, A. Blakers, N. Zin, K. McIntosh, W. Li, Y.-B. Cheng, T. P. White, K. Weber and K. Catchpole, *Adv. Energy Mater.*, 2017, **7**.
36. M. Jaysankar, B. A. L. Raul, J. Bastos, C. Burgess, C. Weijtens, M. Creatore, T. Aernouts, Y. Kuang, R. Gehlhaar, A. Hadipour and J. Poortmans, *ACS Energy Lett.*, 2019, **4**, 259-264.
37. Z. Wang, X. Zhu, S. Zuo, M. Chen, C. Zhang, C. Wang, X. Ren, Z. Yang, Z. Liu and X. Xu, *Adv. Funct. Mater.*, 2020, **30**, 1908298.